January 12, 2010

Version 1.0

1 Introduction

The theory of quantum chromodynamics (QCD) (1) is currently the best description of the fundamental strong force. This theory describes the color interaction between quarks as being mediated by gluons, which are the vector bosons of the strong force. It has been successfully tested in collisions between e^+e^- (2), ep (3), pp (4), and $p\overline{p}$ (5).

One of the basic properties of QCD is that its coupling strength α_s decreases with the energy of the interaction and that, at sufficiently high energies, QCD calculations can be performed using perturbation theory in powers of α_s (6). Currently, these perturbartive QCD (pQCD) calculations are available at a next-to-leading order (NLO) for many processes and, in some cases, at next-to-next-to-leading order (NNLO) approximation. Leading order (LO) calculations, supplemented with parton shower calculations (7), are used in several Monte Carlo event generators (8,9). In addition, matrix element generators which match NLO calculations of rates for QCD processes with a parton shower Monte Carlo event generator are also available (10), but only a limited number of processes have been implemented.

The pQCD calculations result in a small number of partons in the final state, while experimenters observe "jets" of particles. These jets retain the kinematic properties (energy and momentum) of the parent partons (quarks or gluons). In order to facilitate comparison between data and calculation, jet finding algorithms have been devised that are insensitive to the difficult-to-calculate low

energy phenomena that govern the transition from low-multiplicity partons to high-multiplicity particle final states. There are several jet finding algorithms and the details of the measurements are sensitive to that choice.

While events in which jets are created are used for a detailed understanding of the strong force, it is also possible that such events could also reveal new physical phenomena, including quark substructure (compositeness), extra spatial dimensions and new particles which decay into jets. Because of their high energy, jets can probe very small distances. At the Tevatron, the highest p_{T} jets can probe distances down to $\mathcal{O}(10^{-17})$ cm.

In 2001, the Fermilab Tevatron $p\overline{p}$ collider commenced its Run II, with a collision energy of 1.96 TeV. This energy is higher than the $1992-1996$ Run I energy of 1.8 TeV. Even this relatively small increase in energy leads to a substantial increase in jet production with large transverse momentum, p_{T}, by about a factor of three at $p_{\mathrm{T}} = 500$ GeV/c. The beam intensity is much higher than Run I due to the addition of the Main Injector and the Recycler Ring to the Fermilab accelerator complex. In addition, both the CDF (11) and DØ detectors (12) were upgraded. The results reported here utilize an order of magnitude higher integrated luminosity than reported previously (5).

2 Perturbative QCD

The theory of QCD describes the behavior of those particles (quarks q and gluons g) that experience the strong force. It is broadly modeled on the theory of Quantum Electrodynamics (QED), which describes the interactions between electrically-charged particles. However, unlike the electrically-neutral photon of QED, the gluons, the force-mediating bosons of the strong interaction, carry

the strong charge. This fact greatly increases the complexity in calculating the behavior of matter undergoing interactions via the strong force.

The mathematical techniques required to make these calculations can be found in textbooks (e.g. (13)). Instead of giving an exhaustive description of those techniques here, we focus on those aspects of the calculations employed most frequently in the experimental analysis, thereby clarifying the phenomena experimentalists investigate.

At high energies, the strong interactions between two hadrons can be factorized into three components: (a) the probability of finding the partons in the hadrons, (b) the interaction between quasi-free partons, and (c) fragmentation and hadronization of the final state partons. The process is schematically shown in Figure 1. The cross section of the hadron-hadron scattering with 4-momenta P_1 and P_2 can be written as (13) :

$$\sigma(P_1, P_2) = \sum_{i,j} \int dx_1 \int dx_2 \; f_i(x_1, \mu_F^2) f_j(x_2, \mu_F^2) \hat{\sigma}_{ij}(p_1, p_2, \alpha_s(\mu_R^2), Q^2/\mu_F^2, Q^2/\mu_R^2) \tag{1}$$

The hard interaction between partons i, j is given by $\hat{\sigma}_{ij}$ where $p_1 = x_1 P_1$ and $p_2 = x_2 P_2$ are 4-momenta of the two partons. It is independent of the incoming hadrons' structure and can be calculated using pQCD. The function $f_i(x, \mu_F^2)$ is the probability of finding a parton i with momentum fraction x at the scale μ_F, and is called the parton distribution function PDF. The sum i, j is over the partons in the two respective hadrons. α_s is the strong coupling constant. μ_R is the renormalization scale, which is used to remove non-physical infinities inherent in fixed-order calculations. Q is the characteristic scale of the interaction and is related to some physical scale in the interaction, such as the p_{T} of the leading jet.

This factorization of hadron-hadron interactions into a short distance interaction (hard interaction) and a large distance interaction (PDFs) is done at an arbitrary energy scale μ_F. A parton emitted below the scale μ_F is considered to be part of the hadron structure and thus is described by the PDFs. The hadron structure is measured by many different experiments, especially lepton-hadron scattering experiments. The PDFs are determined by fitting these data and parametrized at a scale μ_0. The QCD evolution equations (7), currently available at NNLO in perturbation theory, are used to evolve these PDFs to any different scale μ. The cross section is a convolution of the PDFs and the parton level cross section and, to be consistent, both must be calculated to the same order in perturbation theory. A complete calculation, including all orders in the perturbation series, must be independent of μ_F, but a fixed order calculation depends on this choice. To evaluate the sensitivity to μ_F, it is usually varied up and down by a factor of two. Scale dependencies are expected to decline with the addition of higher order terms in the calculation.

In Figure 2, for jet production, examples of leading order (LO) and next-to-leader order (NLO) Feynman diagrams are shown. At NLO, the jet cross section receives contributions from virtual corrections to the two parton final state, and from real corrections from the three parton final state. Both contributions are divergent, but the sum is finite. One sees that a NLO pQCD calculation can describe up to three jets in the final state. For inclusive jet production, many different implementations of NLO pQCD calculations are available (14–17). All these programs use Monte Carlo integration techniques to calculate the real and virtual contribution to the cross sections. The EKS program (14) calculates the cross sections for user-predefined cuts on transverse momentum and rapidity

ranges. JETRAD (15) and NLOJet++(16) generate parton events with weights (both positive and negative) and thus full event kinematics are available to the user for jet clustering, detector acceptance calculations and study of any other distribution. These programs require a huge amount of CPU to reach the desired precision. A large fraction of this CPU is consumed in evaluating the PDFs. In the FastJet program (17), the convolution in Equation 1 is modified to a product of a perturbatively calculable piece, calculated using NLOJet++, the strong coupling constant, and a function $F_a(x_1, x_1, \mu_F)$ which depends on only the PDFs and the factorization scale μ_F. The function F_a is calculated on a grid of different values of x_1, x_2, and μ_F only once and interpolated between those points while evaluating the full cross section. This procedures significantly speeds up the calculations.

Near threshold, the phase space for the emission of real gluons is limited and large logarithmic corrections to the above cross section calculation may arise from the incomplete cancellation of infrared divergences against the virtual gluon emission contributions. For jet production, these corrections are expected to contribute at very high x, where parton distributions are falling very steeply. For the inclusive jet cross section, these threshold corrections have been calculated to NNLO at next-to-leading-logarithmic accuracy (18) and are found to be small. However, the corrected cross section shows a substantial reduction of the scale μ_F, μ_R dependence.

The partons radiate when they pass through a color field. In this type of radiation, two forms dominate, collinear and soft radiation. Collinear radiation is in the direction of parent parton, while soft radiation is just low energy emission. These soft and collinear radiation can be calculated in a leading-logarithmic

approximation to all orders and this algorithm is a crucial component of event generators. In this formulism, a gluon radiates another gluon or converts into a $q\bar{q}$ pair according to DGLAP (Dokshitzer-Gribov-Lipatov-Altarelli-Parisi) splitting functions (7) which depend on α_s and a variable z which describes the energy sharing between two daughter partons. Similarly, a quark or an anti-quark can radiate a gluon which radiates further. This sequential radiation results in a shower of partons. The radiation process is continued until the parton virtual mass t is smaller than a mass scale t_0. This simple procedure is augmented by angular ordering, i.e. each subsequent emission is required to have a smaller angle, to simulate color coherence effects. Color coherence leads to suppression of soft gluon radiation in certain regions of phase space. In the final state showers, the radiation is limited to a cone defined by color flow lines and the emission angle at each branch point is smaller than the previous emission angle. Partons with a virtual mass $t \leq t_0 \sim 1$ GeV$/c^2$ are combined into hadrons using a phenomenological hadronization model. The hadronization models have been tuned to reproduce the jet structure observed at e^+e^- colliders. The showering process described above is used for radiation from outgoing partons and called final state radiation (FSR). For radiation from incoming partons, initial state radiation (ISR), the event generators use so-called backward evolution. First the momentum fractions x_1, x_2 of partons participating in the hard interaction are determined. Then, the parton shower that preceded the hard interaction is subsequently reconstructed, evolving partons from the hard interaction scale Q backward in time towards smaller Q where the PDF f is evaluated. The color coherence in initial state radiation is slightly more complicated but still follows the same angular ordering. Interference between initial state and final state radi-

ation is implemented in HERWIG but not in PYTHIA. The independent variable, t, which is how the evolution of $\alpha_s(t)$ is parametrized, is not unique. In the PYTHIA showering algorithm, the squared mass m^2 of the branching parton is used as the evolution variable. HERWIG uses $t = m^2/(2z(1-z))$ where $z = E_b/E_a$ is ratio of daughter parton energy (E_b) to the parent parton energy (E_a). In recent versions of PYTHIA, the option of $t = p_{\rm T}$ of the branching parton is also available as the evolution variable.

Occasionally, the radiated parton is at a sufficiently large angle to the parent parton and carries enough energy that it leads to an identifiable jet. Because these jets are typically of lower $p_{\rm T}$, it does not dominate the event kinematics. However, this lower p_T radiation becomes important in studies of jet multiplicity. This part of ISR/FSR can be considered as a part of the hard scatter $\widehat{\sigma}_{ij}$ or treated independently. For instance, we see in Figure 1 two boxes surrounding the hard scatter. The dashed box surrounds the leading order scatter, while the dotted box surrounds a next-to-leading order diagram. At NLO pQCD, one parton emitted from either incoming or outgoing parton is part of the short distance hard cross section $\widehat{\sigma}_{ij}$. In LO event generators, these parton emissions are treated quasi-independently of the hard scatter and are part of leading-log showering process.

The partons from the incoming hadrons which do not participate in the hardest scatter in an event also interact, but these interactions are normally soft. The particles produced in these multi-parton interactions are, on average, isotropically distributed in the allowed $y - \phi$ (19) space and can overlap with the jets produced in the hard interactions. Being soft, multi-parton interactions are in the non-perturbative regime and thus are implemented in event generators using phe-

nomenological models. The parameters of these multi-parton interaction models have been tuned to reproduce the transverse energy and multiplicity distributions of the particles observed far away from the hard jets in collider data (20,21). The beam remnants, the partons which do not participate either in hard or multi-parton interactions, go along the beam direction. However, they do carry color and to become color-singlets, they must exchange (soft) partons with the rest of the event. The particles produced in multi-parton interactions and from the hadronization of beam remnants collectively constitute the underlying event.

As described above, pQCD predictions for jet production are available at NLO at the parton level only. These predictions can not, in principle, be compared directly with the data which is available at the particle level, because these parton level calculations do not include hadronization effects and the contribution from the underlying event. On the other hand, event generators include hadronization, underlying event energy, and ISR/FSR to all orders in the leading-log approximation, but the hard interaction is calculated at LO only. Thus to compare data with QCD predictions, a hybrid scheme is generally used. The parton level NLO calculations are correcting for the underlying event and hadronization effects before they are compared with data. These corrections are determined using Monte Carlo event generators by comparing the jets obtained by clustering the pQCD partons with the jets obtained by clustering the partons after the showering process. The parton jets are obtained from the Monte Carlo events in which the underlying event simulation (multiple parton scattering) has been turned off.

Over the last decade, there has been a lot of progress in simulating high jet multiplicity events using tree-level matrix elements. In ALPGEN (22), events with the exclusive parton multiplicities $n = 2, 3, 4,$ and 5 are generated using matrix

elements from pQCD at the tree level. To include the effect of soft and collinear emission to all orders (albeit in the leading-log approximation), these events are passed through a showering program e.g. in PYTHIA. The phase spaces of the matrix elements and the parton showering program overlap. In particular, showering programs occasionally generate hard partons which can lead to a state which has already been generated by the matrix element. To avoid this double counting, a matching criteria is used. For example, in ALPGEN it is required that the number of jets produced by clustering the partons produced by the matrix element is the same as those produced after the showering for $n \leq 4$. The events which do not satisfy this condition are rejected. For the $n = 5$ parton state, the showering algorithm is allowed to produce a higher jet multiplicity state. The spectra from each different multiplicity are combined to form the full spectrum. In SHERPA (23), a different matching procedure (24) is used where parton showers above a cut off k_{T}-like measure (c.f. Equation 4) are vetoed. Both ALPGEN and Sherpa have been extensively tested at the Tevatron in W/Z+jet production, but these studies are not discussed here due to space constraints (25).

While lepton-nucleon deep inelastic scattering (DIS) experiments are able to precisely measure the quark content of the proton, this precision is not achievable for the gluon, especially at high x. At low x, the gluon distribution can be determined precisely using QCD scaling violation in DIS data. Studying the high-x gluon distribution functions requires data from hadron-hadron scattering. The effect of including Tevatron jet data in global fits to determine PDFs is described in Section 5.3.

3 Jet Clustering Algorithms

Because a parton carries the strong charge, it is not directly observable. It showers into many partons which combine together to form a large number of particles which travel in roughly the same directions as the initial parton. The kinematic properties of the initial parton can be inferred either from the shower of partons or from the jet of collimated particles. For this inference, these particles or partons must be clustered into a *jet* by an algorithm. In pQCD, at NLO and higher orders, a jet algorithm is needed to define physics observables which are well-defined i.e. they are soft/collinear safe. Jet algorithms are run on a few partons generated in pQCD calculations to construct such variables. Experimentally, the final state particles are observed as tracks in the tracker systems or as towers of energy in the calorimeter. These tracks or towers must also combined in a jet so that they can be compared to the parton produced in the hard interaction. In the following, we will collectively call the (a) partons in a pQCD calculation, (b) partons or (c) particles produced in Monte Carlo event generators, or (d) towers or (e) tracks, or (f) reconstructed particles observed in a detector as the *objects* which are input for a clustering algorithm.

For a valid comparison between observations and theoretical predictions, the clustering algorithm must satisfy some basic criteria (26,28). The algorithm must be safe against soft (infra-red IR) and collinear radiation, invariant to boosts along the beam direction, and should be insensitive to the non-perturbative hadronization effects. In an algorithm which is not safe against soft/collinear radiation, the virtual and real contributions in pQCD calculations do not cancel completely and thus the predicted cross sections are ill-defined. One should be able to run the same algorithm on the detector calorimeter towers or tracks,

particles or the multi-parton state from event generators and partons in fixed order pQCD calculations and get sensible results. Experimentally, jet clustering algorithms should be insensitive to the energy from additional hadron-hadron collisions in the same bunch crossing which overlaps the energy from hard interactions, and should not consume too much computer resources such as CPU. Finally, the algorithm must be completely specified to avoid different interpretations.

Commonly used jet-finding algorithms can be divided into two categories: (a) cone clustering and (b) pair-wise recombination algorithms. With a few exceptions, only cone clustering algorithms have been used at hadron colliders. The cone clustering algorithms used prior to the Tevatron Run II were not IR/collinear safe (26, 27), and it was proposed to add an additional seed at the midpoint of stable cones. This made the new algorithm IR/collinear safe to NLO for the inclusive jet cross section measurement. For other physics observable, it is either safe at LO only or unsafe at all orders (28). Various issues related to jet reconstruction are extensively discussed in a recent review (29).

3.1 Cone Clustering Algorithm

For jet studies in Run II, both the CDF and DØ collaborations are using the Midpoint algorithm, as laid out by the QCD Workshop recommendations (26), but the two implementations differ in some details. Below we describe the implementation of this algorithm by the CDF collaboration.

The clustering process starts by making a list of all objects to be clustered. In simulated events, all the particles or partons are included without a p_{T} threshold. However, in data, the calorimeter towers are required to have $p_{\mathrm{T}} \geq 100$

MeV/c to minimize the effect of noise. From this list, a second list of seed objects is made with the requirement that the p_{T} of the objects exceeds a fixed threshold of 1.0 GeV/c. At each seed location, the 4-momentum of the cluster is determined by summing the 4-momenta of all the objects within a distance $R = \sqrt{(y - y_c)^2 + (\phi - \phi_c)^2}$ from the seed (y_c, ϕ_c). The 4-momenta are summed using the E-scheme (26),

$$(E, p_x, p_y, p_z) = \sum_i (E, p_x, p_y, p_z)_i \tag{2}$$

$$p_T = \sqrt{p_x^2 + p_y^2} \qquad y_c = \frac{1}{2} \ln \left(\frac{E + p_z}{E - p_z} \right) \qquad \phi_c = \tan^{-1}(p_y/p_x). \tag{3}$$

This scheme is different from the Snowmass scheme (30) used in Run I, where the clustering centroid was defined as the E_T-weighted average of η and ϕ. Using the center of the cluster as a new seed location, the process is iterated until the center of the circle (y_c, ϕ_c) coincides with the position of cluster 4-momentum.

After all the stable cones have been identified beginning with real seeds, there is an additional search for stable cones using as seed locations the midpoints between the initial set of stable cones. The cone finding algorithm allows that the same object may be part of many cones. The shared objects are uniquely assigned to a single cone using a split-merge algorithm as specified in (26). If two stable cones share objects, the shared energy is compared to the energy of the energy of the lower p_{T} cone. If the ratio of the shared energy to the energy of the lower p_{T} cone is higher than the energy fraction f_{merge}, the two cones are merged. Otherwise, based on proximity, the shared objects are assigned to the nearest cone. The two collaborations use different values of f_{merge}: CDF (DØ) uses $f_{merge} = 0.75$ (0.50). This split-merge procedure may lead to jets which are not circular in $y - \phi$ space. After all the objects above threshold have been

uniquely assigned to a stable cone, the jet kinematics are determined using the same E-scheme.

A cone clustering algorithm can be made infrared safe to all orders if a stable cone is evaluated at each point in $y - \phi$ space. Such an algorithm is very CPU-intensive even when the number of particles is modest and thus is not practical beyond some parton level pQCD calculations. Recently, a new seedless cone clustering algorithm has been proposed which is infra-red and collinear safe to all orders in perturbation theory. The Seedless Infrared Safe Cone SISCONE algorithm (31) uses the fact that a circle enclosing a set of particles can be moved around such that two of the particles lie on its circumference. Consequently, all stable circles can be reconstructed by considering all possible pairs of particles. After determining all the stable circles h, the algorithm merges and splits the stable circles to uniquely assign the particles to a single circle. This algorithm is fast and has been used at the Tevatron for comparison purposes only.

3.2 Pairwise Clustering Algorithm

The cone algorithm combines all the objects within a distance R from the seed. In contrast, the recombination algorithms combine pairs of objects based on some measure d_{ij} and is an attempt to "undo" the showering of partons. The k_{T} algorithm (32,33) starts with a list of proto-jets given by 4-momentum (E, p_x, p_y, p_z). All the objects which are to be clustered are considered as proto-jets. The transverse momentum p_{T}, rapidity y, and azimuthal angle ϕ of a proto-jet are calculated using Equation 3.

For each proto-jet i and the pair $(i, j,\ i \neq j)$, d_i and d_{ij} are defined as

$$d_i = p_{T,i}^2 \qquad d_{ij} = \min(p_{T,i}^{2p}, p_{T,j}^{2p})\ \frac{(y_i - y_j)^2 + (\phi_i - \phi_j)^2}{D^2} \tag{4}$$

where D is the parameter which controls the size of the jet. For the k_{T} algorithm, the parameter $p = 1$. The algorithm determines the minimum d_{min} of the d_i and all the d_{ij}. If $d_{min} = d_i$, the proto-jet is not mergable and is promoted to a jet. Otherwise, the proto-jets i, j are merged into a single proto-jet with the 4-momentum $(E_{ij}, \vec{p}_{ij}) = (E_i + E_j, \vec{p}_i + \vec{p}_j)$. The process is repeated until no proto-jets are left.

The k_{T} algorithm has been extensively used at e^+e^- and ep colliders. At hadron colliders, the environment is more challenging. The energy from multi-parton interactions and beam remnants and pile-up can contribute to the jets and must be taken into account. The large particle multiplicity observed in hadron-hadron collisions requires substantial CPU resources to process an event. Thus the use of the k_{T} algorithm has been limited at hadron colliders. The DØ collaboration measured the inclusive jet cross section in Run I (34). In the Tevatron Run II, the k_{T} algorithm has only been used by the CDF Collaboration to measure the inclusive jet cross section (described in Section 5.2).

Recently, two more recombination algorithms using $p = 0$ (Cambridge-Aachen) (35) and $p = -1$ (anti-k_{T}) (36) in Equation 4 have been proposed. The Cambridge-Aachen algorithm combines particles based only on their relative distance. The anti-k_{T} algorithm combines the highest p_{T} objects in the events first. This leads to circular jets, which have well-defined area like the cone jets. Thus far, these algorithms have not been used at the Tevatron.

4 Jet Energy Scale Determination

At the Tevatron, jets are generally measured using a calorimeter, which is sensitive to both charged and neutral particles. Both CDF and DØ utilize sampling

calorimeters, which measure only a small fraction of the energy of the particles. This observed energy is multiplied by a calibration constant so that it is equal to the sum of the energies of the incident particles. The calorimeter response is different for hadrons, photons, electron and muons. For hadrons, the response depends on the momentum and the flavor of the particles, whereas for photons and electrons it is almost momentum-independent. Muons normally deposit a little energy (~ 1 GeV) in the calorimeter, which is almost independent of the muon momentum. Neutrinos escape without interacting and lead to an imbalance in the measured p_{T} in the event. The observed jet energy must be corrected for the calorimeter response and other detector effects. The two collaborations employ different techniques to determine these jet energy scale corrections. The CDF collaboration's technique (37) depends on an accurate modeling of the calorimeter response to single particles and a knowledge of the p_{T} spectrum of the particles in a jet, whereas the DØ technique is data-driven and utilizes the fact that in photon-jet events $p_{T,Jet} = p_{T,\gamma}$ (38). These techniques are used to calibrate the central region of the calorimeter where the tracking system is available to measure the charged particle momentum and also the calorimeter response is uniform.

This approach was applied in the optimum calorimeter region for both collaborations. The calorimeter response was extended to other regions ($0.1 < |\eta|$, $|\eta| > 0.7$ for CDF and $|\eta| > 0.5$ for DØ), by using dijet balancing to scale the jet energy response in the other regions to the one in the optimum region. The energy from additional $p\bar{p}$ interactions in the same bunch crossing is subtracted, based on the number of reconstructed primary vertices in an event. For cone jets, this correction is determined from minimum bias events by summing the energy in towers in a cone of radius R placed randomly in the calorimeter. The

procedure for k_{T} jets is described in Section 5.2.

Photon-Jet balancing: In this technique, the jet energy is determined by scaling the measured jet p_{T} to the photon's p_{T} in photon-jet events. The photon energy is measured by the electromagnetic (EM) calorimeter which is linear and has very good energy resolution. In the approximation of $2 \rightarrow 2$ scattering, the jet transverse energy p_{T} is equal to the photon p_{T}. The real situation is a little more complicated due to presence of initial state radiation ISR, the energy not clustered in the jet, and contributions to the clustered jet from the multiple parton interactions. To be insensitive to these effects (especially ISR), DØ evaluates the missing p_{T} ($\not\!\!E_T$) projection fraction along the photon direction using:

$$R_{had} = 1 + \frac{\vec{\not\!\!E}_T \cdot \vec{p}_{T,\gamma}}{p^2_{T,\gamma}} \tag{5}$$

The hadronic recoil correction factor, R_{had}, is the scale factor to the entire recoil system. By requiring that the jet is back-to-back with the photon and, in the absence of any additional jet(s) in the event, R_{had} is almost equal to the jet response. The derived response is expressed in the jet energy E' determined from the p_{T} of the photon and the position of the balancing jet using $E' \equiv p^{\gamma}_{\mathrm{T}}/\sin\theta^{\mathrm{jet}}$as both p^{γ}_{T} and the direction of the jet are accurately measured and thus E' provides a better estimate of the jet energy than the direct jet energy measurement by the calorimeter. It is preferred over jet p_{T}, as the calorimeter response depends on the energy of the incident particles and thus parametrization of calorimeter response in E' is more natural.

The EM calorimeter is calibrated using the electrons from Z boson decays such that the reconstructed Z boson mass is equal to the world average (39). The EM calorimeter response to electrons and photons is similar, but not the same, as

photons start their shower later than electrons. This difference is small and is evaluated using simulated events at $p_{\mathrm{T}} = 100$ GeV/c. The estimated uncertainty on the photon energy scale is 0.5% at low E' and 0.8% at high E'. Using this procedure, the DØ collaboration has achieved a 1% accuracy on the jet energy scale in photon-jet events. The current statistics of the γ+jets sample limit the direct measurement of the jet energy corrections in the central region to $E' < 350$ GeV. The response is extrapolated to higher energies using Monte Carlo, which has been tuned to the data. The correction to a single jet with a given algorithm and size is deduced from R_{had} using simulated events.

The calorimeter response to jets depends on their flavor, as the particle spectrum and multiplicity for quark-initiated and gluon-initiated jets are different. The jet energy scale corrections determined from γ+jet events is valid only for the flavor composition of γ+jet events. Event topologies with different flavor composition will have different jet energy scale corrections. Indeed, DØ tuned the single-pion response in their detector simulator to data and used PYTHIA to generate photon-quark, photon-gluon and dijet events. They found that the gluon jet response was 8(2)% lower for jets with 20(500) GeV of energy. In QCD jet production, the fraction of gluon-initiated jets changes with jet p_{T} and the corrections were adjusted to account for this variation in flavor composition. With these additional corrections, the uncertainty on the jet energy scale is reduced to an unprecedentedly-small value.

Jet Corrections using Single Particle Response: Another approach to determine the jet energy correction is based on a knowledge of the calorimeter response to each particle that makes up a jet. The CDF collaboration measured

the calorimeter response to charged hadrons and electrons using both $p\bar{p}$ collider and test beam data. The calorimeter simulation was tuned to reproduce the measured response. The calorimeter response to a jet was determined by a convolution of the single particle response with the type and momentum distribution of particles constituting a jet as given by a fragmentation model. CDF used QCD dijet events with the PYTHIA fragmentation model to measure the default jet corrections. The PYTHIA fragmentation model agreed well with the particle p_{T} and multiplicity distributions in a jet measured in $p\bar{p}$ data. The HERWIG event generator was used to crosscheck the PYTHIA fragmentation functions and the results determined using two generators were found to agree well. In this procedure, the difference in calorimeter response to gluon-initiated and quark-initiated jets is automatically included. Although this procedure requires a detailed knowledge of the calorimeter response and a well-tuned simulation, it has the advantages that the correction can be easily determined for any event topology over the entire kinematic range, and real and simulated data have the same corrections and thus can be treated on an equal footing.

5 Inclusive Jet Cross Section

The inclusive jet cross section measurement (40–45) has been used to test QCD and to search for physics beyond the Standard Model by searching for an excess of events at large p_{T}. During Run I at $\sqrt{s} = 1.8$ TeV, the search was limited by both theoretical and experimental systematic uncertainties even with an integrated luminosity of 100 pb^{-1}. The uncertainty on the jet energy scale dominated the experimental uncertainty. NLO pQCD calculations (14–16) significantly reduced the dependence on the factorization and renormalization scales and the

remaining dependence is $\sim 10\%$ and almost independent of jet p_{T} for $p_{\mathrm{T}} > 100$ GeV/c. The jet cross section is not very sensitive to non-perturbative hadronization effects. The underlying event contributes approximately 1 GeV/c of p_{T} to a jet and thus is significant only at low p_{T}. The main theoretical uncertainty arises from uncertainty in the parton distribution functions, especially for large x gluons. Unfortunately, inclusive jet production is the only process in which the high x gluon distribution can be directly measured. The other possible process, photon-jet production, has a limited reach in x and the associated theoretical uncertainties are large. The gluon distributions are also measured from lepton-proton scattering data through QCD scaling violations, but these measurements are also limited to low x values. Because of these limitations, the Run II inclusive jet cross section has been primarily used to constrain the gluon content of the proton. The data at high y are particularly useful as it probes high x at lower Q values where the contribution of physics beyond the Standard Model, if any, is negligible.

Due to the higher center of mass energy and much larger integrated luminosity, Run II jet measurements extend the jet spectrum to higher jet p_{T} compared to the Run I measurements, by approximately 200 GeV/c. Both collaborations implemented an improved jet clustering algorithm. The jet clustering algorithms used in Run II are IR/collinear safe at least to the order of the available pQCD calculations. An accurate determination of the calorimeter response from the $p\bar{p}$ data and also a refinement in the techniques to determine the jet energy scale have lead to reduced uncertainty compared to Run I. In previous inclusive measurements, the hadronization effects were ignored as they were much smaller than both the experimental and theoretical uncertainties. In Run II, both collabora-

tions have evaluated the effect of hadronization and corrected the parton level pQCD calculation. In addition, the pQCD calculations are corrected for the energy from the underlying event, determined using tuned event generators. In contrast, in Run I energy from the underlying event was removed from jets in data.

The CDF collaboration measured the inclusive jet cross section using the cone clustering (46) with cone size $R = 0.7$ and the k_{T} clustering algorithm with $D = 0.4, 0.7$ and 1.0 (47). The DØ collaboration has recently published the inclusive jet cross section (48) using cone clustering algorithm with cone size $R = 0.7$. These three measurements are described below.

5.1 Measurement using Cone Clustering Algorithm

5.1.1 DØ Collaboration The DØ collaboration analyzed 0.7 fb^{-1} of data taken during $2004 - 2005$ to measure the inclusive jet cross section for $p_{\mathrm{T}} > 50$ GeV/c in six rapidity bins, $|\Delta y| = 0.4$ wide, over the range $0 < |y| < 2.4$. The data was collected by triggering on a jet passing a p_{T} threshold. Six triggers with p_{T} thresholds of 15, 25, 45, 65, 95, and 125 GeV/c were used to collect data. Due to high production rates, only predetermined fractions of the lower threshold triggers were recorded. The efficiency for triggering on jet events was measured using data collected with a muon trigger which did not rely on calorimeter activity. These different jet triggers were combined to form the full p_{T} spectrum with each trigger contributing to a unique p_{T} range. Only those data for which the trigger efficiency is $> 98\%$ are used. The events were required to have a reconstructed primary vertex and the position of the $p\bar{p}$ interaction be within 50 cm of the detector center along the beam direction. This requirement

ensured that the jets follow the projective geometry of the calorimeter and thus their energy was accurately measured. The consequence of this requirement was a reduction of only $7.0 \pm 0.5\%$ in the integrated luminosity. The primary vertex was reconstructed using charged particle tracks measured using silicon micro-strip and scintillating fiber detectors located inside a solenoidal magnetic field of 2 T (12).

The triggered data includes events containing cosmic ray interactions, beam halo and detector noise. These contributions are mostly asymmetric and lead to a large imbalance in the momentum in the plane transverse to beam direction, $\not\!\!E_T$. In contrast, for QCD jet production, $\not\!\!E_T$ is ideally zero, apart from a small neutrino contribution. In QCD events, $\not\!\!E_T$ arises mainly from fluctuations in calorimeter response and is much smaller than the total energy observed in the detector. Most of these background events are removed by requiring the ratio of $\not\!\!E_T$ to the transverse momentum of the leading jet to be small. Remaining backgrounds are removed by requiring that the shape of energy deposition in the calorimeters be consistent with the expected shape from a hadronic jet. The shape of energy deposition for a jet is very different from the energy deposited by a cosmic muon or a beam halo particle, as a jet consists of many particles. These shape requirements also remove photons and electrons. These requirements are highly efficient for the signal and the remaining background is estimated to be $< 0.1\%$.

The measured p_{T} of each jet is corrected for calorimeter non-linearity and energy lost in uninstrumented regions. These average jet-by-jet energy corrections do not correct the smearing (bin-to-bin migration) of jets due to the finite energy resolution. This smearing is determined using an iterative procedure. It

is assumed that the particle level physics (true) spectrum is described by the function

$$F(p_{\mathrm{T}}, y) = N_0 \left(\frac{p_{\mathrm{T}}}{100\,\mathrm{GeV/c}} \right)^{\alpha} \left(1 - \frac{2p_{\mathrm{T}} \cosh(y_{\mathrm{min}})}{\sqrt{s}} \right)^{\beta} \exp(-\gamma p_{\mathrm{T}}), \tag{6}$$

where y_{min} is the rapidity lower bin edge. This functional form is a good representation of the NLO pQCD prediction and fits the measured raw inclusive jet spectrum well. This true spectrum is smeared using the jet energy resolution function, which is determined using $p\bar{p}$ collider dijet data and simulated dijet events. The resulting smeared spectrum is compared with data using a χ^2 test. The process is iterated to determine the best parameters $(N_0, \alpha, \beta, \gamma)$ of the true function, $F(p_{\mathrm{T}}, y)$. This true spectrum is used to correct the migrations between bins in p_{T} in the observed data. In the central region, the migration correction is a multiplicative factor that is $0.8 - 0.9$ at low p_{T} and 0.7 at higher p_{T}, with a strong dependence on y. The true spectrum $F(p_{\mathrm{T}}, y)$ is measured separately for each rapidity bin. The jet rapidity is measured very precisely and thus migration between rapidity bins is small. The y migration corrections are less than 2% in most bins and 10% in the highest p_{T} bin where spectrum is the steepest. The rapidity unsmearing is applied after the p_{T} unsmearing. After the jet energy scale and resolution smearing corrections, the observed data distribution has been corrected to the particle-level jets and is completely independent of the detector properties.

The observed inclusive particle jet spectrum compared with the NLO pQCD predictions, corrected for underlying event and hadronization effects, is shown in Figure 3. The NLO pQCD predictions are calculated using NLOJet++ and FastJet (16, 17) which use α_s^3 matrix elements with $\mu_R = \mu_F = p_{\mathrm{T}}^{\mathrm{jet}}$. The parton distribution functions from CTEQ6.5M (49) are used, which include the Run I

inclusive jet data. The dashed curve shows the NLO pQCD prediction calculation using MRST 2004 divided by the same calculated using CTEQ6.5M. The experimental uncertainty, dominated by the jet energy scale uncertainty, is 12% at $p_{\mathrm{T}} = 50$ GeV/c and 17% at $p_{\mathrm{T}} = 550$ GeV/c in the $|y| < 0.4$ bin. The uncertainty is higher in other y bins. These results are the most precise to-date. The main theoretical uncertainties arise from the uncertainty on the PDFs and the missing higher order terms in the perturbation series. As is customary, the effect of higher order terms is evaluated by varying the renormalization and factorization scale. Fortunately, the change in cross section from varying these scales is almost independent of the p_{T} of the jets. The predicted cross section changed by $\sim 10 - 15\%$ when the scale is changed to $\mu = 2p_{\mathrm{T}}$ or $\mu = p_{\mathrm{T}}/2$. There is a good agreement between the data and the theoretical predictions over the whole p_{T} range which spans 50 GeV/c to 550 GeV/c. Over this p_{T} range, the cross sections falls by 10 orders of magnitude.

The data prefers the lower bound of the theoretical prediction, favoring a smaller gluon content of the proton at high x. The theoretical uncertainty arising from the uncertainties in the parton distribution functions is larger than the experimental uncertainties. These data, along with CDF inclusive jet data, have been used in the global fits to improve the precision of the gluon distribution function. The results of these fits are described in Section 5.3.

5.1.2 CDF Collaboration The CDF collaboration measured the inclusive jet cross section for a cone size of $R = 0.7$, using slightly more data, corresponding to $1.13\,\mathrm{fb}^{-1}$ (46). The measurement spans five rapidity bins $|y| < 0.1$, $0.1 < |y| < 0.7, 0.7 < |y| < 1.1$, $1.1 < |y| < 1.6$, $1.6 < |y| < 2.1$. These bins are matched to the CDF calorimeter structure (11) and thus are different than

the binning used in DØ analysis. The data was collected between $2002 - 2005$ using jet triggers with four thresholds: 20, 50, 70 and 100 GeV/c. In order to not saturate the data acquisition system by jet triggers, only 1/808, 1/35, 1/8 of lower threshold triggers were recorded. The transverse energy of each jet is corrected on average to form the jet p_{T} spectrum which was corrected for bin-to-bin migration of jets due to finite jet energy resolution. CDF used simulated events to evaluate the smearing corrections. The corrections depend on the shape of the true jet p_{T} spectrum and the jet energy resolution. A large sample of QCD jet events was generated using the PYTHIA event generator (8) and passed through the CDF detector simulation. The detector simulation was tuned to describe the single particle response measured in $p\bar{p}$ collisions (37). These simulated data were analyzed using the same procedure as the one used for the real data to obtained the smeared spectrum. The bin-to-bin migration effect was determined by taking the ratio of smeared jet spectrum and the particle jet spectrum. For this procedure to be valid, the smeared p_{T} spectrum of the simulated events must match the spectrum measured in data. The two spectra are very close but not exactly same. The simulated particle jet smeared p_{T} spectrum was adjusted (re-weighted) to force it to agree with the measured spectrum. Re-weighting changes the unsmearing corrections by only a few percent. The unsmearing correction is $< 5\%$ for $p_{\mathrm{T}}^{\mathrm{jet}} < 300$ GeV/c and increases to as much as 20% at $p_T = 500$ GeV/c.

The corrected jet p_{T} spectrum is compared to perturbative QCD predictions evaluated with the FastNLO (17) program using the CTEQ6.1M parton distribution functions (50). The renormalization and factorization scales (μ_R, μ_F) are chosen to be $p_{\mathrm{T}}/2$, which are the same as used in the global QCD analysis to determine the PDFs (50). Using $\mu_R = \mu_F = p_{\mathrm{T}}^{\mathrm{jet}}$ gives up to 10% smaller predictions

in the cross section. The perturbative QCD predictions are corrected for underlying event and hadronization effects measured using the procedure described in Section 2. While clustering the partons produced by the FastNLO, CDF used an ad-hoc parameter R_{sep} which was introduced to mimic the split and merge procedure in iterative cone clustering algorithms (51). At order α_s^3, the final state can have up to three partons. Depending on their relative p_{T} and their separation in $y - \phi$ space, these partons are clustered into two or three jets, Two partons are clustered into a single jet if they are within R from the jet centroid and within $R \times R_{sep}$ of each other. A value of $R_{sep} = 1.3$ is used in this calculation. An $R_{sep} = 2.0$ (i.e. the midpoint algorithm without R_{sep}) yields less than a 5% increase in cross section for NLO QCD predictions. As shown in Figure 4, the data are in good agreement with the theoretical predictions. The experimental uncertainty, dominated by the jet energy scale uncertainty, is comparable to the theoretical uncertainty which is dominated by the PDF uncertainty.

5.2 Measurement using the k_{T} Clustering Algorithm

The k_{T} clustering algorithm, which combines objects in pairs to reconstruct a jet, is infra-red and collinear safe at all orders in perturbation theory and is preferred over iterative cone algorithms. The CDF collaboration has measured (47) the inclusive jet cross section using the k_{T} clustering algorithm with $D = 0.4, 0.7,$ and 1.0 using 1.0 fb^{-1} of data in the same rapidity region as used in the cone-based analysis (46). The analysis procedure is similar to the one described in Section 5.1.2, except the correction for multiple-interactions which are determined using a novel approach. The measured jet transverse momenta are corrected for this effect by removing a certain amount of transverse momentum, $\delta_{p_{\mathrm{T}}}^{mi} \times (N_V - 1)$

where N_V denotes the number of primary vertices in the event. The value of $\delta_{p_{\rm T}}^{\rm mi}$ was determined by requiring the shape of the $p_{\rm T}$ spectrum at high instantaneous luminosity ($\mathcal{L}^{\rm inst}$) to be the same as the one at the low $\mathcal{L}^{\rm inst}$. After making the shape of two spectra the same, the data at low $\mathcal{L}^{\rm inst}$ and high $\mathcal{L}^{\rm inst}$ are combined. The study was carried out independently for each rapidity region and the results were consistent with a common value $\delta_{p_{\rm T}}^{\rm mi} = 1.86 \pm 0.23$ GeV/c. The corresponding correction for the cone jets is 0.97 ± 0.29 GeV/c, which is measured by summing the $p_{\rm T}$ in a cone of $R = 0.7$ in minimum bias events.

The $p_{\rm T}$ spectra are compared in Figure 5 with NLO QCD predictions using the CTEQ6.1M PDFs (50) with $\mu = 0.5 \times p_{\rm T}^{\rm maxjet}$ for $D = 0.7$. The theoretical predictions are calculated using the JETRAD (15) program. The data are in very good agreement with QCD predictions except in the highest rapidity bin ($1.6 < |y| < 2.1$), where the data are lower than the prediction, but well within experimental systematic uncertainties. The theoretical uncertainties are dominated by the PDF uncertainties and are comparable or larger than the experimental uncertainties. The theoretical predictions using the MRST2004 PDFs is very close to those based on the CTEQ6.1M PDFs, except in the $1.6 < |y| < 2.1$ bin, where the MRST2004 cross section is smaller, but within the PDF uncertainty on the CTEQ6.1M prediction. The results for jet size $D = 0.4$ and $D = 1.0$ show similar behavior.

The jet $p_{\rm T}$ spectra measured using two different clustering algorithms are expected to be different and can be compared only via theoretical predictions. The ratios of data/theory from two analyses were compared and the two ratios were in very good agreement with each other except in the $0.7 < |y| < 1.1$ region where the $k_{\rm T}$ cross section is $\sim 5\%$ higher. In this y region, the CDF calorimeter

coverage is not uniform which leads to a large variation in calorimeter response and poor jet energy resolution. The two CDF analyses have similar experimental uncertainties. Thus one concludes that both the k_{T} and the cone clustering algorithms can be successfully used at the hadron colliders.

5.3 Determination of Gluon Distribution Function

The parton distribution function (PDF) $f_i(x, \mu)$, which is the probability to find a parton with a type $i = g, q, \bar{q}$ with momentum fraction x and mass scale μ, must be experimentally determined. The PDFs for gluons and light quarks and anti-quarks $(u, d, s, \bar{u}, \bar{d}, \bar{s})$ are normally determined from experimental data. For heavier quarks, i.e. c and b, they are normally dynamically generated through gluon splitting. Data from $e^{\pm}p$ collisions at the ZEUS and H1 experiments (3), νp, $\bar{\nu}p$, νn, $\bar{\nu}n$ collisions at CCFR/NuTeV (52), and Drell-Yan (lepton pairs and W/Z bosons) production in pp (53) and $p\bar{p}$ collisions (54), jet data from Tevatron and data from many other experiments, especially low energy, are used to extract the PDFs using a global fit. These experiments are sensitive to different f_i. For example, $e^{\pm}p$ experiments are sensitive to the sum of the q and $\bar{q}$ distributions weighted by $e^2_{q(\bar{q})}$ and can not distinguish between quark and anti-quark distributions. Neutrino and anti-neutrino data are used to differentiate between q and $\bar{q}$. The Tevatron jet data play a significant role in constraining the gluon distribution at large x. The gluon distribution at low x are mainly determined from the scaling violations in lepton-nucleon scattering data. Normally, the results of these global analysis are fit at some initial scale μ_0 using tens of parameters. The PDF can be evolved to any arbitrary scale μ using QCD evolution equations which are available at NNLO approximation in perturbation theory.

Both the MSTW (55) and CTEQ (56) collaborations have included Run II jet data in their global analysis to update the PDFs. The three Run II inclusive jet measurements are more accurate than Run I measurements, span a larger p_{T} range and are consistent with each other (55). As two CDF measurements used the same data, the MSTW collaboration decided to use the k_{T} jet spectrum whereas the CTEQ collaboration is using the cone-based measurements. The Run I jet measurements do not play a significant role in the fit and thus the MSTW collaboration has dropped those data from the new fits. Comparisons of the gluon distribution $g(x)$ determined in the new MSTW fit with the gluon distributions from MRST2004 (57) and CTEQ6.6 (58) fits along with the 90% uncertainty band are shown in Figure 6 (left) for $\mu^2 = Q^2 = 10^4$ GeV^2. The new $g(x)$ is lower than previous fits for $x \geq 0.3$ but within the still large systematic uncertainties. As α_s and $g(x)$ always appear as a product, the values of α_s and $g(x)$ are strongly correlated. The value of α_s in the three sets of PDFs is different and thus $g(x)$ is also expected to be slightly different. The fractional uncertainty on the gluon distribution is shown in Figure 6 (right). At $x = 0.4$ and $\mu^2 = 10^4$ GeV^2, the uncertainty reduces from 18% when the jet data are excluded from the fit to 12% when jet data are included in the fit. This modest extra constraint will make the predictions more precise at the LHC in processes where gluon-quark scattering dominates.

5.4 Determination of the strong coupling constant

The hard cross section for jet production ($\widehat{\sigma}_{ij}$) in Equation (1) at large p_{T} can be expanded in powers of the strong coupling constant to the nth order in per-

turbation theory

$$\widehat{\sigma}_{ij} = \alpha_s^2 \sum_{m=0}^{n} c_{ij}^{(m)} \alpha_s^m. \tag{7}$$

where the perturbative coefficients $c_{ij}^{(m)}$ are functions of the kinematic variables and the factorization scale only. The coefficients $c_{ij}^{(m)}$ are available for $m = 0$ and $m = 1$. Using the jet cross section measurement, the strong coupling constant α_s can be determined using Equation 1 provided the parton distributions functions are known. This technique was used by the CDF collaboration to measure α_s at different p_{T} values and show its running with the hard scattering scale in Run I (59). In Run II, the DØ collaboration has used the same principle but an improved technique to measure α_s (60) from the data used to measure the inclusive jet cross section. These data were corrected for hadronization and underlying event using PYTHIA. The hadronization (underlying event) corrections vary between -15% (+30%) to -3% (+6%), for $p_{\mathrm{T}} = 50$ GeV/c to 600 GeV/c (48).

The perturbative results are the sum of $\mathcal{O}(\alpha_s^3)$ pQCD calculation (16,17), supplemented with $\mathcal{O}(\alpha_s^4)$(2-loop) corrections for the threshold effects (18). The PDFs are taken from the MSTW2008 next-to-next-to-leading order (NNLO) parametrization and the renormalization and factorization μ_R, μ_F scales are set equal to the p_{T} of the jet. The MSTW2008 PDFs are available for 21 different values of $\alpha_s(M_Z)$ ranging from 0.110 to 0.130 in steps of 0.001. This α_s is used to evolve PDFs.

Commonly available parton distributions from the MSTW and CTEQ groups include Tevatron jet data in the global fit. To avoid any correlation between the input PDFs and the extracted α_s, only 22 of 110 available jet data points are used. These selected points contribute to the x region ($x \leq 0.25$) where PDFs in global fits are mainly determined by other experimental data and are not strongly

influenced by Tevatron jet data. The jet data starts to affect $g(x)$ at $x \sim 0.2$. The change in $g(x)$ due to inclusion of jet data is less than 5% for $x \lesssim 0.25$ (55).

The central $\alpha_s(M_Z)$ result is obtained by minimizing χ^2 with respect to $\alpha_s(M_Z)$ and integrating over the nuisance parameters for the correlated uncertainties. The variation of $\alpha_s(p_{\mathrm{T}})$ vs p_{T} is shown in Figure 7 (top). The running of α_s as a function of jet p_{T} follows the QCD evolution equation. The data points from the H1 and ZEUS experiments follow the same curve but have large uncertainties. The α_s, evolved to $\mu = M_Z$, is shown in Figure 7 (bottom). The combined result of 22 selected points $\alpha_s(M_Z) = 0.1161^{+0.0041}_{-0.0048}$ is consistent with the world average 0.1184 ± 0.0007 (61) although the uncertainties, mostly theoretical, are large.

6 Search for Physics Beyond the Standard Model using Jets

Due to large theoretical and experimental uncertainties in the jet production rate, the high p_{T} tail cannot be used to improve upon the current limits on new interactions (62). However, there are kinematic distributions from jet events that can be used to identify physics beyond the Standard Model. Below we describe these searches using the dijet mass spectrum and the dijet angular distributions. These searches are not very sensitive to the jet energy scale, parton distribution functions or renormalization or factorization scales.

6.1 Dijet Mass Spectrum

Many new physics models predict particles which decay into two high p_{T} jets. These particles can be identified by the reconstructed mass of the dijet system provided their intrinsic mass width is narrow. Such models include excited quarks (63), axigluons (64), flavor-universal colorons (65), color-octet techni-

ρ (66), Randall Sundrum (RS) gravitons (67), heavy vector bosons (68) and diquarks in the string-inspired E_6 model (69). The excited quarks q^* decay into qg. Heavy vector bosons W', Z' decay into $q\bar{q}$ or $q\bar{q}'$. The axigluon A decays into $q\bar{q}$, and E_6 diquarks $D\,(D^c)$ decay into $\bar{q}\bar{q}(qq)$. The RS Graviton G^* and color-octet techni-ρ ρ_{T8} both decay into either a qq or gg pair but their branching ratios are different.

All these models predict an intrinsic mass width which is much smaller than both the detector resolution and mass broadening effects due to QCD radiation. These models can be divided into three categories depending on the decay channel, i.e. gg, gq and qq. The expected mass shapes for q^*, G^*, W', and Z' particles with a mass of 800 GeV$/c^2$ are shown in Figure 8. Because q^* and G^* decay into gluons, their widths are broader than the widths for W' and Z'. Gluons radiate more than quarks, resulting in a broader dijet mass distribution. These distributions are close and change the final limits by only 10-20%. These shapes can be used to search for resonance structure, independent of the model details.

To measure the dijet mass spectrum (70), the CDF collaboration used the same data set as used in the inclusive jet cross section measurement described in Section 5.1.2 (46). The dijet mass is reconstructed from the two highest p_{T} jets using

$$m_{jj} = \sqrt{(E_1 + E_2)^2 - (\vec{p}_1 + \vec{p}_2)^2}. \tag{8}$$

Jets produced by new physics are expected to be produced more centrally than by Standard Model processes and we expect a better signal to background ratio in the central region. Thus only those events in which two leading jets have $|y| \leq 1.0$ are used. Moreover, the CDF calorimeter is best understood in this region. As shown in Figure 9, these data, after all corrections, are in good agreement with

the NLO QCD calculations. The dijet mass spectrum before smearing corrections is shown in Figure 10. Smearing corrections are not used to avoid any degradation of the resonant structure, if any, in the data. The measured mass spectrum is fit to a smooth background given by

$$\frac{d\sigma}{dm_{jj}} = p_0(1-x)^{p_1}/x^{p_2+p_3\ln(x)}, \qquad x = m_{jj}/\sqrt{s}, \tag{9}$$

where p_0, p_1, p_2, and p_3 are free parameters. The dijet mass spectra predicted by PYTHIA, HERWIG, and NLO pQCD can be described well by this functional form. The fit to the measured dijet mass spectrum is shown in Figure 10(a). The data are well described by this smooth function with a χ^2 of 16 for 17 degrees of freedom. The deviation from the smooth curve is shown in Figure 10(b). These data are used to determine the exclusion limits on the existence of new particles decaying into jets, as there is no evidence for the existence of any resonant structure. The experimental limits are determined for the $\sigma^{sig} \equiv \sigma \cdot B \cdot A$, where σ is the theoretical new particle production rate, B is probability of its decaying into two jets and A is the kinematic acceptance of the resulting particle jets to have $|y| < 1.0$.

The upper limits on σ^{sig} are evaluating using a likelihood function

$$L = \prod_i \mu_i^{n_i} \exp(-\mu_i)/n_i! \tag{10}$$

where $\mu_i = n_i^{sig} + n_i^{QCD}$ is the predicted number of events in bin i. The QCD dijet background n_i^{QCD} is determined using Equation (9) by evaluating $\mathcal{L}_i \cdot \epsilon_i \cdot \Delta m_{jj} \cdot d\sigma/dm_{jj}|_i$ where Δm_{jj}, ϵ_i, and $\mathcal{L}_i$, are the bin width, the trigger efficiency and the integrated luminosity for bin i respectively. The expected signal events n_i^{sig} is given by $\sigma^{sig} \cdot \mathcal{L}_i \cdot \epsilon_i \cdot (n_i/n_{tot})$ where ϵ_i is the signal event selection efficiency in the ith dijet mass bin and n_i/n_{tot} is the predicted signal fraction in bin i. For each

value of σ^{sig}, the likelihood is maximized with respect to the four parameters in Equation (9). This profiled likelihood is integrated over Bayesian priors for the parameters describing the systematic uncertainties (71). A flat prior on σ^{sig} is used to extract a Bayesian upper limit on that parameter.

The mass exclusion limits for W', Z', q^* and G^* are determined by comparing the limits obtained using their respective signal shapes and the predicted theoretical cross section. For other models, the limits obtained for the above four signal shapes are used. The q^* signal shape (qg) is used for axigluons, the flavor-universal coloron and the E_6 diquark, as these particles do not decay into modes which include gluons and thus their signal shapes are expected to be narrower than the q^* signal shape. For ρ_{T8}, the limits obtained for the G^* shape are used. Both the ρ_{T8} and the G^* decay into $q\bar{q}$ or gg, but the branching fraction of G^* into gg is higher. Thus in all the above cases, the obtained exclusion limits are conservative. The limits for these models are given in Table 1.

The dijet mass spectrum measured by the DØ collaboration in six rapidity bins (72) is shown in Figure 11. The rapidity bin is labeled by the higher of the two jet rapidities. The data are compared to NLO pQCD predictions computed by NLOJet++ (16) using the MSTW2008 NLO PDFs (55) with scale $\mu_R = \mu_F = (p_{T,1} + p_{T,2})/2$ and are corrected for non-perturbative effects determined using the PYTHIA event generator. The data and QCD predictions are in reasonable agreement for the $|y| < 0.4$ region which is not surprising as the MSTW2008 global fit includes the inclusive jet data (see Section 5.3). For higher $|y|$ bins, the data are below the theoretical predictions but within $1\,\sigma$ of the total experimental systematic uncertainty. The DØ collaboration is searching for new particles using these data.

6.2 Dijet angular distributions

The angle between the initial and final state partons in the center of momentum frame is sensitive to the spin of the exchanged or the intermediate particle and thus can be used to search for physics beyond the Standard Model. At hadron colliders, dijet production is dominated by the t channel exchange of a gluon, a massless vector boson, and the angular distribution has the familiar Rutherford scattering form

$$\frac{d\hat{\sigma}}{d\cos\theta^*} \sim \frac{1}{(1-cos\theta^*)^2} = \frac{1}{\sin^4(\theta^*/2)} \tag{11}$$

where θ^* is the angle between the jet and the beam direction in the dijet center of momentum frame. The angular distribution of the new particles proposed in many new physics scenarios is relatively flat in $\cos\theta^*$. For example, the angular distribution of spin 1 particles (W', Z', Axigluon, coloron) decaying in fermions is $d\sigma/d\cos\theta^* \sim 1 + cos^2\theta^*$ Theories in which quarks are composite particles but with the compositeness scale much higher than the available energy, can be parametrized by an effective Lagrangian of the type (62, 73, 74),

$$\mathcal{L} = \eta\frac{g^2}{4\Lambda^2}(\bar{q}_i\gamma^\mu q_i)(\bar{q}_j\gamma_\mu q_j) \qquad i = L, R,\ j = L, R$$

where Λ is a parameter in the theory which controls the characteristic energy of the new interactions. The parameter η is ± 1 and determines the sign of interference between new interactions and the SM interactions. The main effect of substructure is to increase the proportion of centrally produced jets, which can be observed in the jet angular distributions (73).

The ADD LED models (75, 76), proposed to solve the heirarchy problem, i.e. the difference between electroweak scale ($\sim$ 100 GeV) and the Plank scale M_{Pl} ($= 1/G_F \sim 10^{19}$ GeV), assume the existence of extra spatial dimensions in which

gravity is allowed to propagate. As a consequence, gravity appears weak in the three conventional spatial dimensions. The Planck scale, the number of extra dimension n, their size R and an effective Planck scale M_S are related by $M_{Pl} = M_S R^n$. Experimentally, M_S can be measured for different values of n. The Kaluza-Klein excitations of the graviton can be exchanged between partons and thus contribute to jet production, resulting in jets which are central. There are two different formalisms to describe LED models, GRW (77) and HLZ (78). In the HLZ formalism, the sub-leading dependence on the number n of extra dimensions is also included.

In some models (79–81), extra dimensions are assumed to exist at the TeV^{-1} distance scale. In these models, Kaluza-Klein excitations of SM bosons modify various production cross sections. In these models, gluons can propagate through the extra dimensions, which changes the jet cross section. The strength of the interaction is given by the model parameter, the compactification scale, M_C.

To search for new physics, instead of studying the $\cos\theta^*$ distribution directly, it is convenient to use the χ_{dijet} distribution which removes the Rutherford singularity: χ_{dijet} is defined as $\exp(y_1 - y_2)$ where y_1 and y_2 are rapidities (19) of the two highest p_{T} jets in an event. For $2 \rightarrow 2$ scattering of massless partons, the variable χ_{dijet} is related to the partonic center-of-momentum frame polar angle θ^* by $\chi_{dijet} = (1 + \cos\theta^*)/(1 - \cos\theta^*)$.

The CDF collaboration studied the dijet angular distributions using $106\,\mathrm{pb}^{-1}$ of data from Run I (82). The data excludes at 95% CL a model of quark substructure in which only up and down quarks are composite and the contact interaction scale is $\Lambda^+_{ud} \leq 1.6$ TeV or $\Lambda^-_{ud} \leq 1.4$ TeV where the subscript refers to the flavor of quarks assumed to be composite and the superscript $\pm$ refers to the sign of

the interference. For a model in which all quarks are composite, the excluded regions are $\Lambda^+ \leq 1.8$ TeV and $\Lambda^- \leq 1.6$ TeV. In Run II, the DØ collaboration measured the χ_{dijet} distribution in the $\chi_{dijet} \leq 16$ range in 10 dijet mass m_{jj} bins covering the $0.25 < m_{jj} < 1.1$ TeV/c^2 range using up to 0.7 fb^{-1} of data collected during $2004-2005$ (83). The boost of the two-jet system is required to be $y_{\text{boost}} \equiv 0.5 \times |y_1 + y_2| \leq 1$. This requirement, combined with the dijet mass cut and the range of the χ_{dijet} distribution, restricts the highest allowable rapidity to $|y_{1,2}| < 2.4$ where the DØ detector performance is well understood. The measured distributions are corrected for detector effects using events generated with PYTHIA v6.419 (8) with tune QW (21) and the MSTW2008LO parton distributions functions. This procedure corrects for the migration between dijet mass bins, as well as the shape of the χ_{dijet} distributions in each mass bin. The corrected normalized differential cross section distributions ($1/\sigma_{dijet} \cdot d\sigma/d\chi_{dijet}$) at the particle level are shown in Figure 12 for 10 dijet mass bins. The NLO pQCD predictions are computed using FASTNLO (17) based on NLOJet++ (16). These parton level predictions are corrected for the hadronization and underlying event contributions, which are evaluated using PYTHIA. The theoretical uncertainties on the SM χ_{dijet} distributions arising from the uncertainty on the PDFs and the uncertainty on renormalization and factorization scales are less than 2% and 5% respectively. These data are in good agreement with the SM predictions and thus are used to set exclusion limits in the parameter space of quark compositeness, ADD LED and TeV^{-1} models. Calculations for all these models are available only at leading order, while pQCD calculations can be performed at next to leading order. For this analysis, the expected distributions for each new model are calculated at LO and then scaled by k-factors ($k = \sigma_{\text{NLO}}/\sigma_{\text{LO}}$) determined from

pQCD calculations. The k-factors vary from 1.25 to 1.5. All these models predict a higher rate as $\chi_{dijet} \to 1$ and as m_{jj} increases. However, the magnitude of the excess is different for different models. A Bayesian procedure (84) is used to obtain 95% C.L. limits on the mass scale parameters Λ, M_C and M_S in the above models. The results in which the prior is chosen to be flat in the model cross section are given in Table 2. Other choices give similar but slightly higher limits (83).

The limits on M_C obtained in this analysis are the first direct search for TeV^{-1} extra dimensions at a particle collider, though inferior to indirect limits from precision electroweak measurements (81). The limits on M_S in different formalisms of ADD LED are on average slightly higher than the recent DØ results obtained using dielectron and diphoton data (85). The quark compositeness limits are the most stringent limits to date.

7 Conclusions

Since the start of the Run II, there has been a significant increase in the experimental data used in the jet analyses at the Tevatron. Due to the higher production cross section and the increase in available integrated luminosity, the inclusive jet cross section measurement has been extended to transverse momenta of 600 GeV/c. The experimental uncertainty is still dominated by the uncertainty on the jet energy scale which is +31/-26% in the $p_{\mathrm{T}} = 457 - 527$ GeV/c bin in $0.1 < |y| < 0.7$ region for the CDF measurements and +16.0/-15.5% in the $p_{\mathrm{T}} = 490 - 540$ GeV/c bin in $|y| < 0.5$ region for DØ measurements. Both collaborations used a modern jet finding algorithm, the midpoint algorithm, which is infra-red and collinear safe at next-to-leading order in pQCD for measurements of

the inclusive jet cross section. In addition, the treatment of the underlying event energy and hadronization effects has improved over the techniques used in Run I. The experimental uncertainties are lower than the theoretical uncertainties, which are dominated by the uncertainties on the parton distribution functions. These data have been used in global fits to determine the parton distributions and have decreased the uncertainty on the gluon distribution for the $x \geq 0.3$ region. The new gluon distribution is slightly lower than that determined by Run I jet cross section measurements. This increase in the accuracy of gluon distributions will make the prediction of various processes more precise.

These jet data have been successfully used to search for physics beyond the Standard Model using jet kinematic distributions. The dijet mass spectrum has been used to expand the exclusion regions in parameters of excited quarks in quark compositeness models, E_6 diquarks, axigluons and heavy vector bosons W and Z bosons, and the techi-ρ in color octet models. The 95% C.L. lower mass limits range from 630 GeV/c^2 for colorons to 1.25 TeV/c^2 for axigluons. The dijet angular distribution has been used to extend the limits on the quark compositeness mass scale, ADD large extra dimensions and the TeV^{-1} extra dimensions. The 95% C.L. lower limit on the compositeness mass scale is 2.8 TeV. The 95% C.L. lower limit for compactification mass scale in the TeV^{-1} model is 1.5 TeV. The limits on the ADD large extra dimensions range from 1.9 TeV to 1.3 TeV depending on the number of extra dimensions in the HLZ formalism. The 95% C.L. in the GRW formalism is 1.6 TeV. In most cases, these are the best limits to date.

Literature Cited

1. Gross DJ, Wilczek F Phys. Rev. D 8:3633 (1973); Fritzsch H, Gell-Mann M, Leutwyler H Phys. Lett. B 47:365 (1973); Politzer HD, Phys. Rev. Lett. 30:1346 (1973)
2. Stenzel H Nucl. Phys. B (Proceedings Supplements) 152:23 (2006)
3. Gwenlan C Acta. Phys. Polon. B 35:377 (2004)
4. Fabjan C, McCubbin N Phys. Rep. 403:165 (2004)
5. Blazey GC, Flaugher BL Annu. Rev. Nucl. Part. Sci. 49:633 (1999)
6. Salam GP, arXiv:0906.1736v3 [hep-ph] 2 July 2009
7. Gribov VN, Lipatov LN Sov. J. Nucl. Phys 15:438 (1972); Altarelli G, Parisi G Nucl. Phys. B 126:298 (1977); Dokshitzer Yu Sov. Phys. JETP 46:641 (1977)
8. Sjöstrand T, et al. JHEP 0605:026 (2006)
9. Corcella G, et al. JHEP 0101:010 (2001)
10. Frixione S, Webber BR JHEP 0206:29 (2002)
11. Abulencia A et al. J. Phys. G: Nucl. Part. Phys. 34:2457 (2007)
12. Abazov VM, et al. Nucl. Instrum. Methods Phys. Res. Sect. A 565:463 (2006)
13. Ellis RK, Stirling WJ, Webber BR *QCD and Collider Physics*, Cambridge Press. (1996)
14. Ellis SD, Kunszt Z, Soper DE Phys. Rev. Lett. 64:2121 (1990)
15. Giele WT, Glover EWN, Kosower DA Nucl. Phys. B 403:633 (1993)
16. Nagy Z Phys. Rev. D 68:094002 (2003)
17. Kluge T, Rabbertz K, Wobisch M arXiv:hep-ph/0609285 (2006)
18. Kidonakis N, Owens JF Phys. Rev. D 63:054019 (2001)
19. The important kinematic variables are the rapidity $y = \frac{1}{2}\ln\frac{E+p_z}{E-p_z}$, the az-

imuthal angle $\phi = \tan^{-1}\frac{p_y}{p_x}$ and transverse momentum $p_T = \sqrt{p_x^2 + p_y^2}$ where a particle or jet has a 4-momentum (E, p_x, p_y, p_z) and the positive z is defined by the proton beam's direction, positive y is up and the x direction is that required to make a right-handed coordinate system. In addition, the pseudorapidity $\eta = -\ln[\tan(\theta/2)]$ is sometimes used, where θ is the polar angle, measured with respect to the proton beam axis. The boost rapidity is defined as $y_{\text{boost}} = 0.5|y_1 + y_2|$.

20. Field R, Fermilab ME/MC tuning workshop, Fermilab (2002)
21. Field R et al. (Tev4LHC QCD Working group) arXiv:0610012 [hep-ph] (2006)
22. Mangano ML, et al. JHEP 0307:001 (2003)
23. Gleisberg T, et al. JHEP 0402:056 (2004)
24. Catana S, Krauss F, Kuhn R, Webber BR JHEP 0111:063 (2001); Krauss F JHEP 0208:015 (2002)
25. Ellis SD et al. Prog. Part. Nucl. Phys. 60:484 (2008)
26. Blazey GC et al. Proceedings of the Physics at RUN II: QCD and Weak Boson Physics Workshop, Batavia, Illinois, 4-6 Nov 1999 arXiv:0005012v2 [hep-ex] (2000)
27. Kilgore W, Giele WT Phys. Rev. D 55:7183 (1997)
28. Buttar C, et al. arXiv:0803.0678v1 [hep-ph] (2008)
29. Salam GP arXiv:0906.1833v1 [hep-ph] (2009)
30. Huth JE, et al. FERMILAB-CONF-90-249-E (1990)
31. Salam GP, Soyez G JHEP 0705:086 (2007)
32. Catani S, et al. Nucl. Phys. B 406:187 (1993)
33. Ellis SD, Soper DE Phys. Rev. D 48:3160 (1993)
34. Abazov VM, et al. Phys. Lett. B 525:211 (2002)

35. Dokshitzer Yu, Leder G, Moretti S, Webber B JHEP 9708:001 (1997)

36. Cacciari M, Salam GP, Soyes G JHEP 0804:063 (2008)

37. Bhatti A, et al. Nucl. Instrum. Methods Phys. Res. Sect. A 556:375 (2006)

38. DZero JES PRD, in preparation. **REMAINING PROBLEM This paper is soon to be released. It is a PRD of the earlier Dzero inclusive jet measurement and contains lots of JES information.**

39. Amsler C, et al. Phys. Lett. B 667:1 (2008)

40. Arnison G, et al. Phys. Lett. B 172:461 (1986)

41. Alitti J, et al. Phys. Lett. B 257:232 (1991); Alitti J, et al. Z. Phys. C 49:17 (1991)

42. Abe F, et al. Phys. Rev. Lett. 70:1376 (1993)

43. Abe F, et al. Phys. Rev. Lett. 77:438 (1996)

44. Affolder T, et al. Phys. Rev. D 64:032001 (2001)

45. Abbott B, et al. Phys. Rev D 64:032003 (2001)

46. Aaltonen T, et al. Phys. Rev. D 78:052006 (2008)

47. Abulencia A, et al. Phys. Rev. D 75:092006 (2007)

48. Abazov VM, et al. Phys. Rev. Lett. 101:062001 (2008)

49. Tung WK, et al. J. High Energy Phys. 02:053 (2007); Pumplin J, et al. J. High Energy Phys. 07:12 (2002)

50. Stump D, et al. J. High Energy Physics 10:046 (2003)

51. Ellis SD, Soper DE Phys. Rev. D 48:3160 (1993)

52. Tzanov M Int. J. Mod. Phys. A20:3759 (2005)

53. Towell RS, et al. Phys. Rev. D 64:052002 (2001)

54. Abe F, et al. Phys. Rev. Lett. 81:5754 (1998); Aaltonen T, et al. Phys. Rev. Lett. 102:181801 (2009); Aaltonen T, et al. arXiv:0908.3914v3 [hep-ex]

(2009); Abazov VM, et al. Phys. Rev. D 76:012003 (2007)

55. Martin AD, et al. Eur. Phys. J. C 63:189 (2009)
56. Pumplin J, et al. arXiv:0904.2424v2 [hep-ph] (2009)
57. Martin AD, Roberts RG, Stirling WJ and Thorn RS, Phys. Lett. B 604:61 (2004)
58. Nadolsky PM, et al. Phys. Rev D 78:013004 (2008)
59. Affolder T, et al. Phys. Rev. Lett. 88:042001 (2002)
60. Abazov VM, et al. arXiv:0911.2710 [hep-ex], *to be published in Phys. Rev. D - Rapid Comm.*
61. Bethke S. Eur. Phys. J C64:689-703 (2009)
62. Eichten E, Lane K, Peskin M Phys. Rev. Lett. 50:811 (1983)
63. Baur U, Hinchliffe I, Zeppenfeld D Int. J. Mod. Phys. A 2:1285 (1987); Baur U, Spira M, Zerwas PM Phys. Rev. D 42:815 (1990)
64. Frampton PH, Glashow SL Phys. Lett. B 190:157 (1987); Bagger J, Schmidt C, King S Phys. Rev. D 37:1188 (1988)
65. Chivukula RS, Cohen AG, Simmons EH Phys. Lett. B 380:92 (1996); Simmons EH Phys. Rev. D 55:1678 (1997)
66. Lane KD, Ramana MV Phys. Rev. D 44:2678 (1991); Lane K, Mrenna S Phys. Rev. D 67:115011 (2003)
67. Randall L, Sundrum R Phys. Rev. Lett. 83:3370 (1999); Bijnens J, et al. Phys. Lett. B 503:241 (2001)
68. Eichten E, Hinchliffe I, Lane K, Quigg C Rev. Mod. Phys. 56:579 (1984); *Ibid*, 58:1065 (1986)
69. Hewett JL, Rizzo TG Phys. Rep. 183:193 (1989)
70. Aaltonen T, et al. Phys. Rev. D 72:112002 (2009)

71. Demortier L, in Proceedings of the Conference on Advance Statistical Techniques in Particle Physics, Institute for Particle Physics Phenomenology, University of Durham, UK (2002)

72. (DØ Collaboration), DØ Note 5919-Conf, (2009) *to be published in Phys. Lett. B*

73. Eichten E, Lane K arXiv:9609298v1 [hep-ph] (1996)

74. Lane KD, arXiv:9605257 [hep-ph] (1996)

75. Arkani-Hamed N, Dimopoulos S, Dvali G Phys. Lett. B 429:263 (1998)

76. Atwood D, Bar-Shalom S, Soni S Phys. Rev. D 62:056008 (2000)

77. Giudice GF, Rattazzi R, Wells JD Nucl. Phys. B 544:3 (1999)

78. Han T, Lykken JD, Zhang RJ Phys. Rev. D 59:105006 (1999)

79. Dienes KR, Dudas E, Gherghetta T Nucl. Phys. B 537:47 (1999)

80. Pomarol A, Quiros M Phys. Lett. B 438:255 (1998)

81. Cheung K, Landsberg G Phys. Rev. D 65:076003 (2002)

82. Abe F, et al. Phys. Rev. Lett. 77:5336 (1996)

83. Abazov VM, et al. Phys. Rev. Lett. 103:191803 (2009)

84. Abbott B, et al. Phys. Rev. D 64:032003 (2001)

85. Abazov VM et al. Phys. Rev. Lett. 102, 051601 (2009).

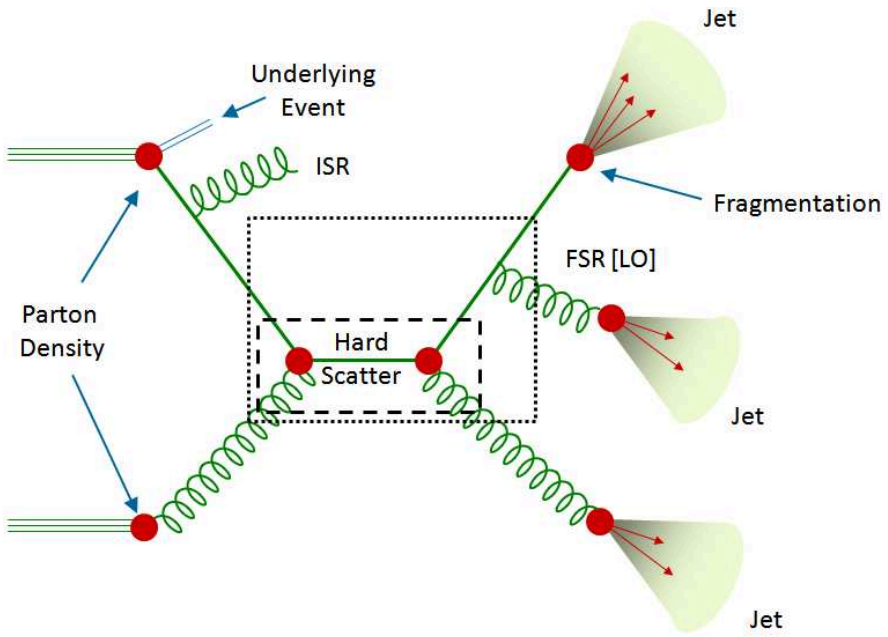

Figure 1: Stylized hadron-hadron collision, with relevant features labeled. Note that a LO calculation of the hard scatter (dashed line) will assign a jet to final state radiation that would be included in the hard scatter calculation by a NLO calculation (dotted line).

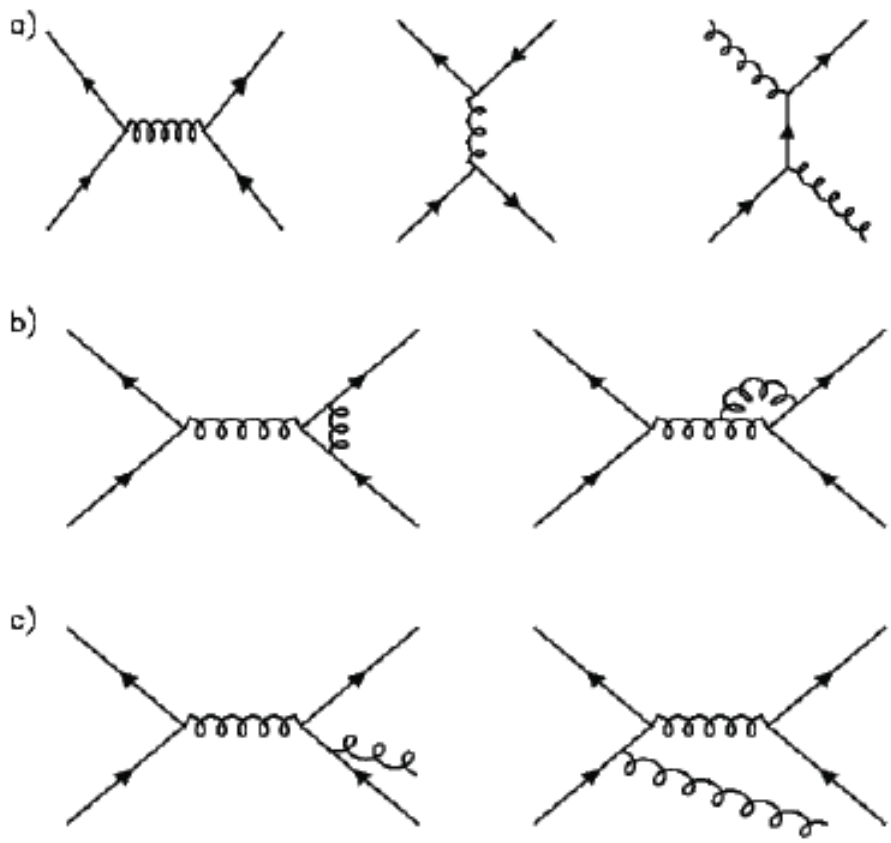

Figure 2: (a) Leading order Feynman diagrams. (b) Next to leading order loop diagrams. (c) Next to leading order tree diagrams.

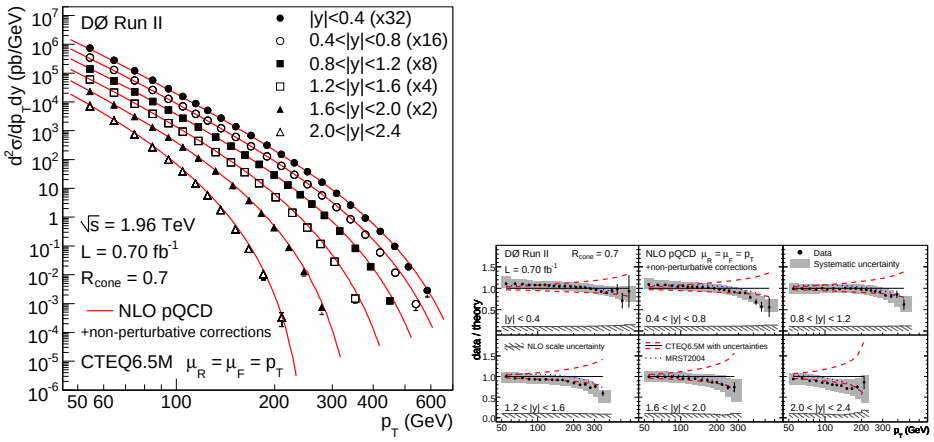

Figure 3: (left) DØ's observed inclusive jet differential cross sections corrected to the particle level in six rapidity regions compared to next to leading order (NLO) QCD predictions (48). The NLO QCD predictions are calculated with the CTEQ6.5M parton distribution functions; (right) ratios of the measured cross sections over the NLO QCD predictions. The data agrees with the theory quite well and has remarkably small systematic uncertainties.

Table 1: The limits on the masses of particles decaying into dijet in various models. Limits are in units of GeV/c^2 (70).

Model	Parameters	Excluded Region
q^*	$f = f' = f_s$	260 - 870
axigluons		260 - 1250
coloron		290 - 630
E_6 diquark		260 - 1100
ρ_{T8}		280 - 840
W'	SM	280 - 840
Z'	SM	320 - 740
G^*	$k/M_{Pl} = 0.1$	-

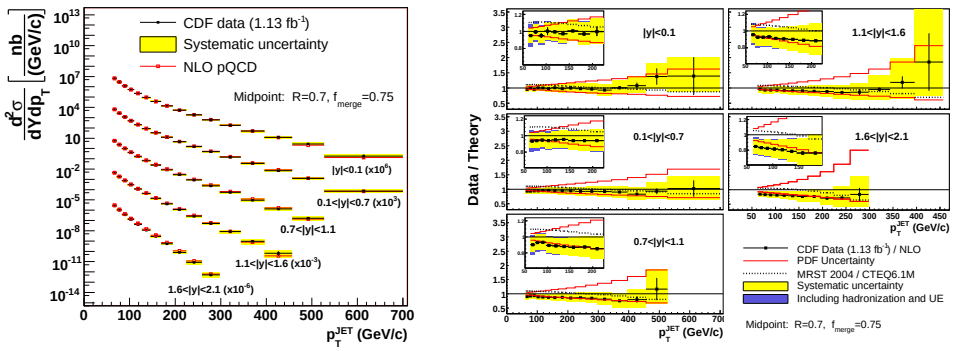

Figure 4: (left) CDF's observed inclusive jet differential cross sections corrected to the particle level in five rapidity regions compared to next to leading order (NLO) QCD predictions (46). The NLO QCD predictions are calculated with the CTEQ6.1M parton distribution functions. (right) Ratios of the measured cross sections over the NLO QCD predictions. The theory describes the data quite well.

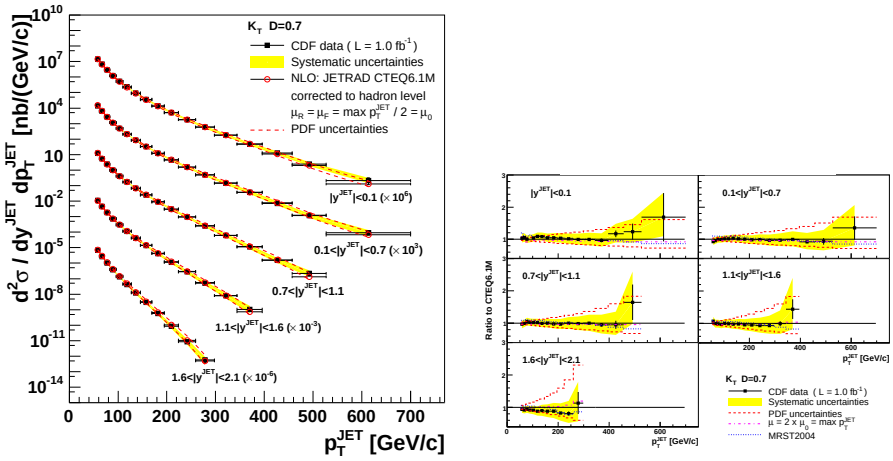

Figure 5: (left) CDF's inclusive jet differential cross sections measured using the k_{T} clustering algorithm in five rapidity regions. The data has been corrected to the particle jets and is compared to next to leading order (NLO) QCD predictions (47). The NLO QCD predictions are calculated with the CTEQ6.1M parton distribution functions. (right) Ratios of the measured cross sections over the NLO QCD predictions. The perturbative NLO QCD calculations are in good agreement with the data.

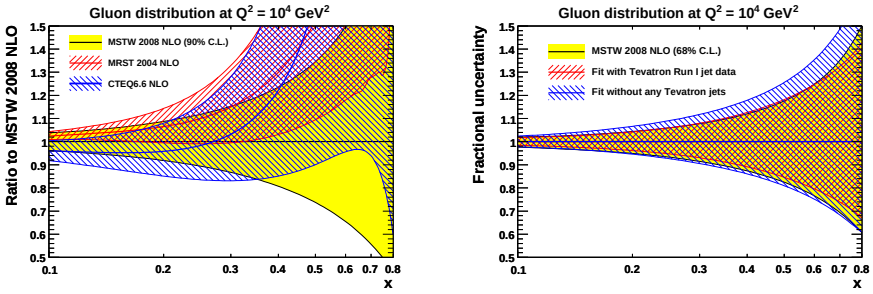

Figure 6: (left) Ratios of various gluon PDFs to the MSTW2008 PDF. (right) The MSTW2008 gluon PDF uncertainties for variations on the inclusion or exclusion of Tevatron data (55).

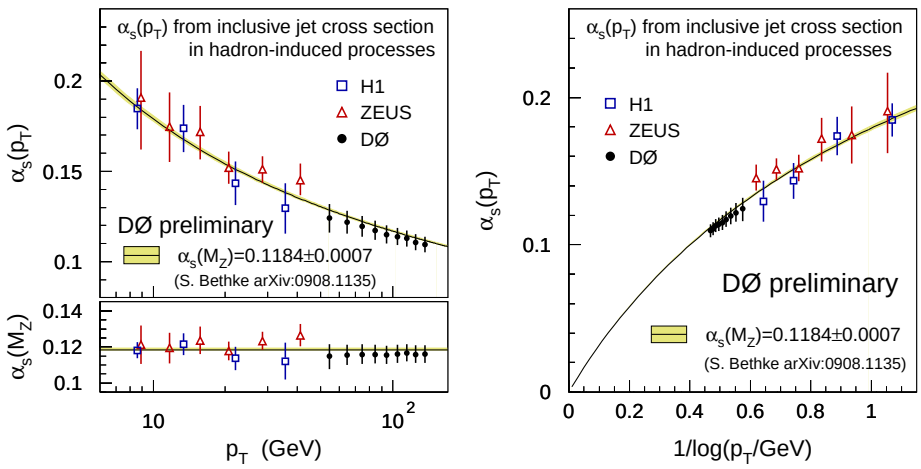

Figure 7: (left) α_s measurement as a function of the transverse momentum of the jet from several experiments, as compared to the expected variation of α_s, setting $\alpha_s(M_Z) = 0.1184 \pm 0.0007$ (60). (right) α_s plotted as a function of $1/\log(p_T)$, which supports the idea of asymptotic freedom.

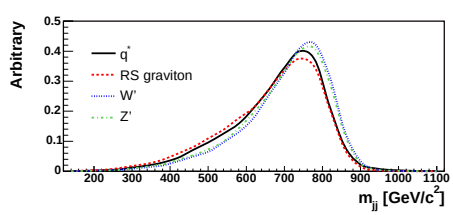

Figure 8: Expected dijet mass distributions for simulated signals for the following new physical models: $q^* \to qg$, RS graviton ($\to gg$, $q\bar{q}$) and $W' \to q\bar{q}$ and $Z' \to q\bar{q}$ with a mass of 800 GeV/c^2.

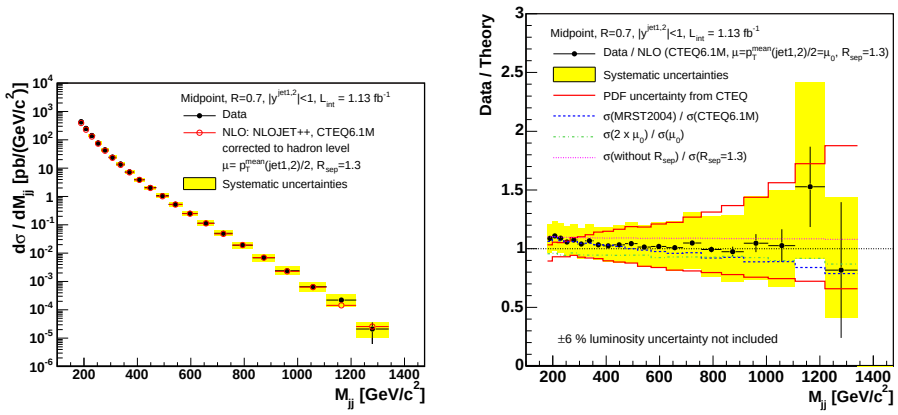

Figure 9: (left) CDF's measurement of the dijet mass cross section for events in which the two highest p_{T} have $|y| < 1.0$ (70) compared to NLO calculations using CTEQ6.1M. (right) Ratio of data to NLO theory. The experimental uncertainties are dominated by jet energy scale uncertainty and are comparable to the theoretical PDF uncertainty.

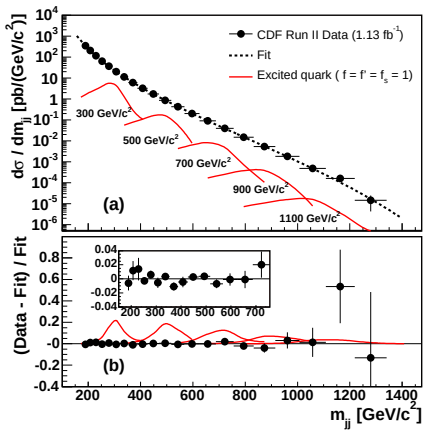

Figure 10: (a) CDF's measured dijet mass spectrum (70). The dashed curve shows the fit to Equation 9. Also shown are the predicted dijet mass distributions of the excited quark q^* for the masses of 300, 500, 700, 900 and 1100 GeV/c^2 respectively. (b) The fractional difference between the measured dijet mass difference and the fit (points) compared to q^* signals divided by the fit to the measured dijet mass spectrum (curves).

Table 2: Expected and observed 95% C.L. limits on various new physics models.

Model (parameter)	Expected (TeV)	Observed (TeV)
Quark Compositeness (Λ)		
$\eta = +1$	2.76	2.84
$\eta = -1$	2.75	2.82
TeV^{-1} ED (M_C)	1.60	1.55
ADD LED (M_S)		
GRW	1.47	1.59
HLZ $n = 3$	1.75	1.89
HLZ $n = 4$	1.47	1.59
HLZ $n = 5$	1.33	1.43
HLZ $n = 6$	1.24	1.34
HLZ $n = 7$	1.17	1.26

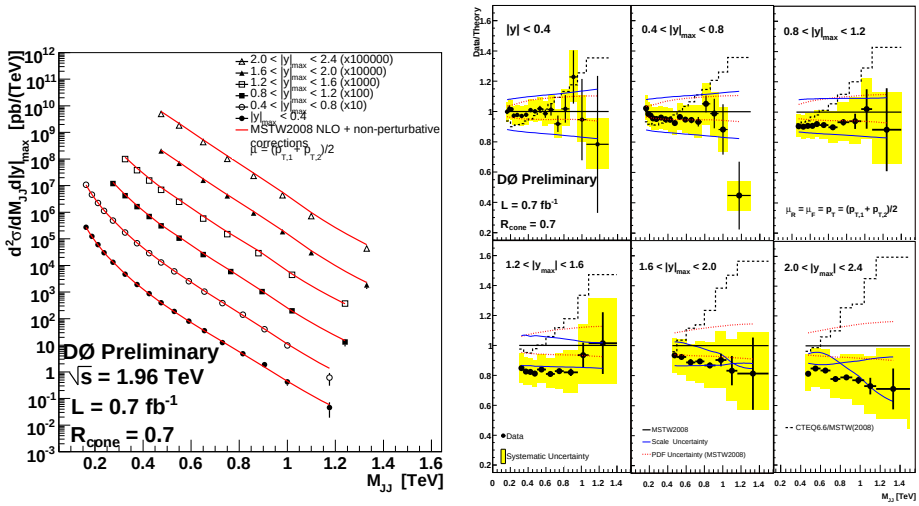

Figure 11: (left) DØ's dijet mass measurement for six rapidity bins (72) compared to NLO using MSTW2008 PDFs. (right) Ratio of data/theory. The experimental systematic uncertainties are very small. The dashed line shows the effect of using the CTEQ6.6M PDFs.

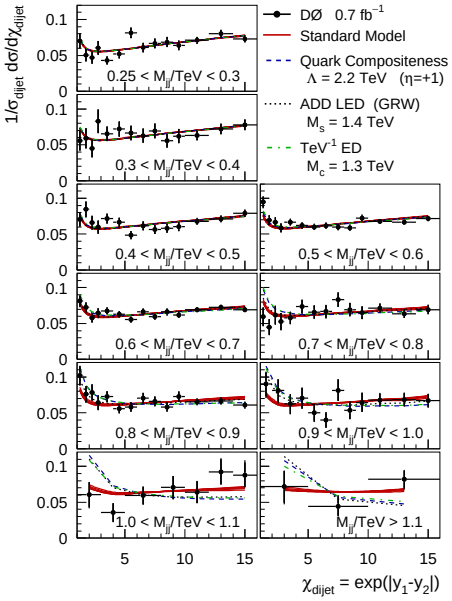

Figure 12: DØ's measurement of the dijet χ for ten dijet mass bins (83). The solid line is the Standard Model prediction at NLO. The dashed lines show the predictions for various new physics models.